





Mapping the multiphase structure of H I in the Low-Latitude Intermediate-Velocity Arch 1

LUKA VUJEVA ^{1,2,3,4} ANTOINE MARCHAL ^{2,5} PETER G. MARTIN ² AND MUKESH TAANK ^{2,6}

¹David A. Dunlap Department of Astronomy and Astrophysics, University of Toronto, 60 St. George Street, Toronto, ON M5S 3H8, Canada

²Canadian Institute for Theoretical Astrophysics, University of Toronto, 60 St. George Street, Toronto, ON M5S 3H8, Canada

³Cosmic DAWN Centre (DAWN), Niels Bohr Institute, University of Copenhagen, Jagtvej 128, DK-2200 Copenhagen N

⁴Niels Bohr Institute, University of Copenhagen, Lyngbyvej 2, DK-2100 Copenhagen Ø

⁵Research School of Astronomy & Astrophysics, Australian National University, Canberra ACT 2610 Australia

⁶Department of Mathematics and Statistics, University of Guelph, 50 Stone Road E., Guelph, ON N1G 2W1, Canada

(Received March 7, 2023; Revised 3 May, 2023; Accepted 6 May, 2023)

Submitted to ApJ

ABSTRACT

We have analyzed the thermal and turbulent properties of the Low-Latitude Intermediate-Velocity Arch 1 (LLIV1). This was accomplished using archival H I emission and absorption data from two 21 cm line surveys: GHIGLS at 9'4 resolution and DHIGLS at 1' resolution. The spectral decomposition code ROHSA was used to model the column density of different thermal phases and also to analyze an absorption measurement against the radio source 4C +66.09. From the latter we found spin temperature $T_s \sim 75$ K, cold gas mass fraction $f \sim 0.5$, and turbulent sonic Mach number $M_t \sim 3.4$. Similar to the absorption line modeling against 4C +66.09, our best emission line decomposition model has no unstable gas across the whole field of view, suggesting that the thermal condensation and phase transition are not on-going but rather have reached an equilibrium state. The cold phase of LLIV1 appears as a collection of elongated filaments that forms a closed structure within the field decomposed. These substructures follow the orientation of the overall large scale cloud, along the diagonal of the GHIGLS field from north-west to south-east (in Galactic coordinates). The angular power spectrum of the cold phase is slightly shallower than that of the warm phase, quantifying that the cold phases have relatively more structure on small scales. Our spatially resolved map of the cold gas mass fraction in LLIV1 from DHIGLS reveals significant variations spanning the possible range of f , with mean and standard deviation 0.33 and 0.19, respectively.

Keywords: Galaxy: halo – ISM: structure - kinematics and dynamics – Methods: observational - data analysis

1. INTRODUCTION

We have surveyed and analyzed the properties of H I line emission in an intermediate latitude field in Ursa Major ($(\ell, b) = (143^\circ.6, 40^\circ.1)$ or $(\alpha, \delta) = (09^h41^m, 68^\circ33')$), focusing on thermal condensation of warm neutral medium gas (WNM) to cold neutral medium gas (CNM) in the intermediate velocity component (IVC). This IVC gas is part of the Low-Latitude Intermediate-Velocity Arch (LLIV) studied by Kuntz & Danly (1996), in particular substructure LLIV1 (see their figure 2). These substructures (or “clumps”) were cataloged by Kuntz & Danly (1996) based on high H I column

density (N_{HI}) contours in the IVC range from data from the Bell Laboratories H I survey at 2° resolution (Stark et al. 1992). LLIV1 has an approximate size of about 10° on the sky and is connected to other substructures through more extended gas with lower N_{HI} (about 10^{19} cm^{-2} in the velocity range $-60 \text{ km s}^{-1} < v < -30 \text{ km s}^{-1}$). Higher resolution N_{HI} maps of LLIV substructures are shown in figures 12(b) and 16 of Wakker (2001), in the velocity range $-60 \text{ km s}^{-1} < v < -30 \text{ km s}^{-1}$ and $-70 \text{ km s}^{-1} < v < -30 \text{ km s}^{-1}$, respectively,

Abundances measurements by Wakker (2001) using lines of SII, NI, and OI indicate a metallicity that is approximately solar. Absorption of Fe and Si against the AGN PG 0804+761 at $(\ell, b) = (138^\circ.3, 31^\circ.0)$ indicates some depletion onto dust grains (Richter et al. 2001). There is thermal dust emission morphologically correlated with the IVC gas

in LLIV (Planck Collaboration XXIV 2011). Wakker (2001) constrain the distance to be in the range 0.9–1.8 kpc ($z = 0.6$ –1.2 kpc). The implied mass is $1.5 - 6 \times 10^5 M_\odot$.

Richter et al. (2003) report a relatively high detection rate of H_2 in the IVC gas, implying that CNM is ubiquitous, consistent with a key finding of our paper. Absorption lines toward PG 0804+761 (Richter et al. 2001) located in the more diffuse part of LLIV at lower Galactic latitudes not analyzed here (Richter et al. 2001, see their figure 1) has an estimated H_2 mass fraction of $\log f_{H_2} = -4.5$. Absorption lines along the line of sight to the distant hot subdwarf PG 0832+675 (Richter et al. 2003) characterize the outer part of the substructure LLIV1 studied here; the fraction of H_2 is somewhat higher ($\log f_{H_2} = -3.9$).

Absorption lines toward PG 0804+761 (Richter et al. 2001) also indicate a substantial ionization fraction for hydrogen, about 20%. There is also hot coronal gas revealed by O VI absorption toward PG 0804+761 (Richter et al. 2001) that could potentially be associated with the highly ionized gas related to the envelope of the LLIV Arch. However, this can also be explained by the presence of hot gas above the Perseus arm, a scenario favored by Richter et al. (2001) due to the presence a Galactic chimney found by Normandeau et al. (1996) in the region where the PG 0804+761 line of sight crosses above the Perseus arm. C IV absorption was also detected toward SN 1993J (de Boer et al. 1993).

Wakker (2001) notes how this is reminiscent of a Galactic fountain (Shapiro & Field 1976; Bregman 1980; Houck & Bregman 1990), where gas ejected into the Galactic Halo from inside the Solar circle is expected to have a metallicity slightly above that in the local ISM, while the return flow is outside the Solar circle. Planck Collaboration XXIV (2011) show that dust appears to survive the hot phases of the flow (or to reform) and discuss the evolution of dust via shattering. What we find most interesting is that there is a substantial CNM apparently organized with the flow.

Some key elements of the structure of the paper are as follows. In Section 2 we present the H I data used in this work. Evidence for cold gas in LLIV1 based on H I absorption is summarized in Section 3. Section 4 describes the Gaussian decomposition performed to model the H I spectra, Sections 4.2 and 4.3 for GHIGLS and DHIGLS, respectively. Appendices A and C present maps (2D spatial fields) characterizing each Gaussian component (column density, central velocity, velocity dispersion) for the respective data. Identification of the different thermal phases is addressed in Section 4.2.2, with attention to the robustness of the solution (Section 4.2.3). Section 4.2.5 presents an angular power spectrum analysis of the phase maps (Section 4.2.4). The cold gas mass fraction map inferred from the decomposition of DHIGLS data is analyzed in Section 4.3.4. Finally, a summary is provided in Section 5.

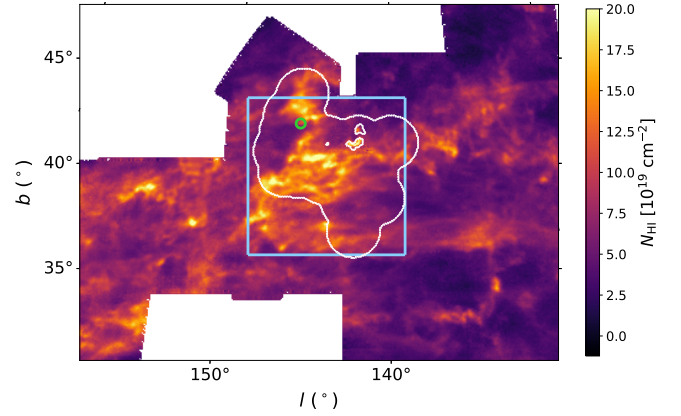


Figure 1. Integrated column density map of the GHIGLS NCPL mosaic in the IVC velocity range $-81 \leq v \leq -27 \text{ km s}^{-1}$ showing the LLIV Arch. The light blue box shows the 128×128 pixel region analyzed. The white contours outline the DHIGLS UM field and its masks (Section 2.2). The green ring marks the direction of the absorption measurement (Section 3).

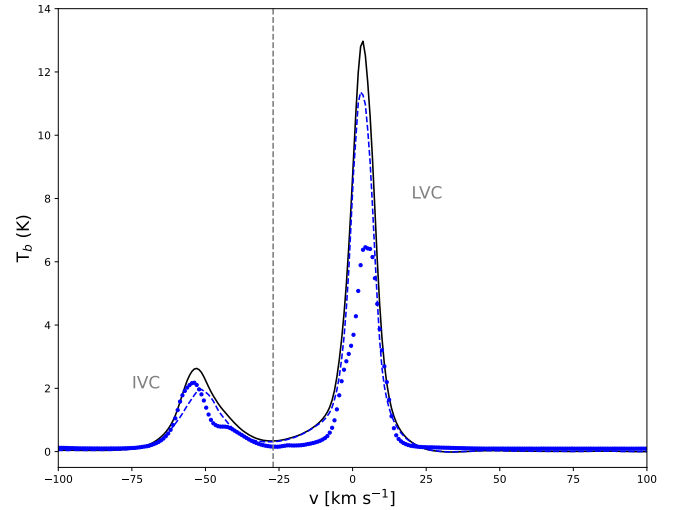


Figure 2. GHIGLS H I spectra characterizing the region analyzed in Ursa Major, the light blue box in Figure 1, showing the LLIV1 and the LVC gas. The black solid, blue dashed and blue dotted lines are the mean, median, and standard deviation spectra, respectively.

2. H I DATA

2.1. GHIGLS (9'4)

We used the GHIGLS¹ 21 cm line survey (Martin et al. 2015) with spatial resolution about 9'4 (pixel size 3'5) and velocity resolution and channel spacing 1.0 km s^{-1} and 0.8 km s^{-1} , respectively, from the Green Bank Telescope (GBT) to examine the brightness temperature T_b of the atomic gas in

¹GBT H I Intermediate Galactic Latitude Survey: <https://www.cita.utoronto.ca/GHIGLS/>

LLIV1. Specifically, we extracted a 7.5 (128 pixels) square sub-region of the NCPL mosaic centered on Galactic coordinates $(144^\circ, +39^\circ)$, the light blue box in Figure 1. The map shows the total integrated column density of the NCPL mosaic in the velocity range $-81 \leq v \leq -27 \text{ km s}^{-1}$ analyzed in this work, covering LLIV1. Following Boothroyd et al. (2011), the rms error in this column density from the 3D line noise (see Section 4.1) is about $0.14 \cdot 10^{19} \text{ cm}^{-2}$ for most of the data analyzed, quite low compared to the signal.² Systematic effects from baseline and stray radiation correction errors could increase this by a factor of three, but these errors do not fluctuate from pixel to pixel and cause the map to look noisy.

Figure 2 shows the mean, median, and standard deviation spectra of data within this sub-region. There is a strong peak near 0 km s^{-1} (hereafter Low Velocity Component (LVC)) that corresponds to gas associated with the NCPL (Taank et al. 2022). The secondary peak near -55 km s^{-1} is the LLIV1 gas. There is also weak emission in the bridge range between the two components. The ranges were divided at $v = -27 \text{ km s}^{-1}$ (denoted by the vertical line) where the emission in the bridge is minimal. Individual channel maps of the mosaic show weak emission in the high velocity range from High Velocity Cloud (HVC) complexes A and C (Planck Collaboration XXIV 2011), extending to velocities close to the IVC range (i.e., $\approx -70 \text{ km s}^{-1}$), but there is very little HVC emission in the region that we analyzed.

For the analysis below, pixels contaminated by extragalactic emission (mainly the M81/82 group) and masked in GHIGLS because of corrupted baselines are in-painted as described in Taank et al. (2022), appendix A.

2.2. DHIGLS ($1'$)

We also made use of the 58 square degrees UM dataset that was part of the DHIGLS³ H I survey (Blagrove et al. 2017) with the Synthesis Telescope (ST) at the Dominion Radio Astrophysical Observatory. This field is located at $(\alpha, \delta) = (09^{\text{h}}41^{\text{m}}, 68^\circ33')$ or $(l, b) = (143^\circ.6, 40^\circ.1)$. The spectra, with channel spacing $\Delta v = 0.824 \text{ km s}^{-1}$ and velocity resolution 1.32 km s^{-1} , cover the range $-70 \text{ km s}^{-1} < v < +30 \text{ km s}^{-1}$. The spatial resolution of the ST interferometric data was about $1'$. UM is embedded in the NPCL mosaic from GHIGLS shown in Figure 1. The DHIGLS UM T_b data cube has the full range of spatial frequencies, obtained by a rigorous combination of the ST interferometric

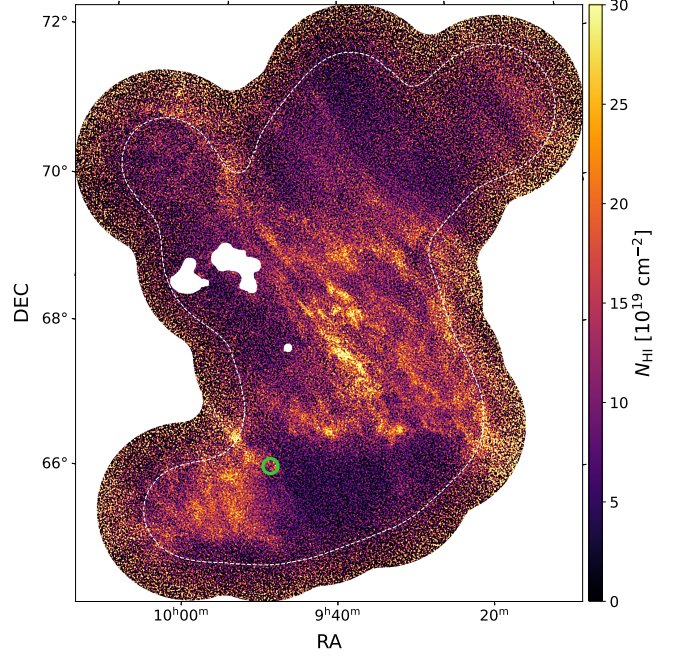


Figure 3. Integrated column density map of the IVC gas in UM from DHIGLS. Given the coverage of ST pointings making up the final UM mosaic, the noise is at a minimum toward the center and increases outward, up by a factor of two at the white dashed contour (see text). The three white regions inside show the masks applied to avoid extragalactic emission. The green ring marks the direction of the absorption measurement (Section 3).

and GBT single dish data (see section 5 in Blagrove et al. 2017). The pixel size is $18''$.

Figure 3 presents the total column density map of the IVC gas in UM (i.e., LLIV1). In this DHIGLS data, the error in brightness temperature (which propagates into the column density error) varies with position, increasing at the edge of the map, tracing back to the primary beam response of the antennae in the ST and the (irregular) geometric arrangement of pointings in the full survey (Blagrove et al. 2017). The white dashed contour shows where the noise has increased by a factor of two relative to the minimum of 1.73 K in a single channel map or about $1.9 \cdot 10^{19} \text{ cm}^{-2}$ in the IVC N_{HI} . The full DHIGLS spatial coverage shown here is annotated by the solid white contour in Figure 1. Note the different native coordinate systems: Equatorial for the DHIGLS data and Galactic for the GHIGLS data. Unlike with the GBT, the higher angular resolution of the ST (i.e., $1'$) allows the detection of high continuum brightness temperature radio point sources, which are useful for H I absorption measurements.

3. EVIDENCE FOR COLD GAS FROM H I ABSORPTION IN LLIV1

Blagrove et al. (2017) reported the detection of CNM gas in the IVC with spin temperature $T_s = 85 \text{ K}$

² Because of duplicate coverage provided by the fields making up the NCPL mosaic, the noise is lower by about a factor $\sqrt{2}$ in the upper left corner and along the right quarter of the field (see the boxy outline of the mosaic in Figure 1 for guidance).

³ DRAO H I Intermediate Galactic Latitude Survey: <https://www.cita.utoronto.ca/DHIGLS/>

Table 1. Parameters^a of the absorption feature in LLIV1 against 4C +66.09, interpolated emission, and derived T_s , f , and M_l , from DHIGLS data

Method	T_c	μ_n	σ_n	T_n	μ_b	σ_b	T_b	T_s	σ_{th}	σ_{nt}	f	M_l
1	444	2.43	1.52	-109	2.67	1.77	22.41	76.3	0.80	1.31	0.51	3.3
2	444	2.43	1.52	-109	2.66	1.99	22.73	72.2	0.80	1.30	0.55	3.4

^a Velocities in km s^{-1} and temperatures in K.

against the background radio galaxy 4C + 66.09 (NVSS⁴ J094912 + 661459) with a continuum brightness temperature $T_c = 444$ K. This gas is located within LLIV1 as annotated in Figure 1 and related figures.

Following Taank et al. (2022), we used the spectral decomposition code ROHSA (Section 4.1) on the original DHIGLS data to model the emission-absorption pair with Gaussians to refine estimates of the spin temperature and the cold component amplitude and turbulent properties.

We found that the absorption spectrum is well described by a single Gaussian component together with a quadratic polynomial to describe the local residual baseline. Parameters μ_n , σ_n , and T_n of the Gaussian are tabulated in Table 1.

The associated emission line was obtained by averaging data in an annulus centered on the source with an inner radius $r_{in} = 1.2$ and an outer radius $r_{out} = 3'$ (i.e., 4 and 10 pixels of size $18''$, respectively). The resulting spectrum is well fit by the sum of two Gaussians, a narrow and a broad component. Parameters μ_b , σ_b , and T_b of the narrow Gaussian are tabulated in Table 1 (method 1). The CNM mass fraction is $f = 0.51$. Following Blagrove et al. (2017), the numbers from Table 1 lead to a spin temperature of $T_s = 76.3$ K, slightly lower than their estimate without profile fitting.

Alternatively, we used ROHSA for a decomposition of emission in a 64×64 pixel grid centered on the source. Again, two Gaussians were needed to fully encode the signal. Parameters μ_b , σ_b , and T_b of the narrower Gaussian at the position of the source were interpolated from the ROHSA parameter maps in the same annulus and are also tabulated in Table 1 (method 2). The CNM mass fraction is $f = 0.55$ and the spin temperature evaluates to $T_s = 72.2$.

Following the procedure described in Taank et al. (2022, see their section 5.1.2), for the CNM line we separated the thermal and non-thermal broadening, σ_{th} and σ_{nt} , respectively, and calculated the associated turbulent Mach number M_l . These are also tabulated in Table 1 for methods 1 and 2.

The inferred properties of cold H I gas in LLIV1 confirms the existence of cool atomic gas clumps in the LLIV Arch that was predicted by Richter et al. (2001) based on the H₂

excitation temperature $T_{0,1} = 193^{+322}_{-75}$ K found along the line of sight to PG 0804+761. They speculated that $T_{0,1}$ might be representative of the gas kinetic temperature because of thermalization by collisions in a dense cold gas predominantly in the atomic phase (i.e., CNM), the fraction of gas in the molecular phase being low.

4. SPECTRAL DECOMPOSITION

To go beyond this single measurement and map out the distribution of cold gas in part of LLIV, specifically LLIV1, we have decomposed emission line data at high resolution from GHIGLS and DHIGLS.

4.1. ROHSA

ROHSA is a regularized optimization algorithm that decomposes position-position-velocity (PPV) data cubes into a sum of Gaussians (Marchal et al. 2019). ROHSA takes into account the spatial coherence of the emission and its multi-phase nature to perform a separation of different thermal phases. The methodology used in this work is similar to that used in Taank et al. (2022). We refer the reader to their section 3 for a comprehensive description of ROHSA and its user-parameters, including the number of Gaussians N and the set of hyperparameters $(\lambda_a, \lambda_\mu, \lambda_\sigma, \lambda''_\sigma)$. A ROHSA decomposition requires the user to choose this set of parameters to obtain a practicable solution and this must be revisited for a given data set (e.g., Marchal et al. 2021; Taank et al. 2022).

Also needed is a noise prescription for the data. For GHIGLS data, we adopted the 3D prescription discussed by Boothroyd et al. (2011), $S(v, \mathbf{r}) = S_e(\mathbf{r})(1 + T_b(\mathbf{r})/T_{sys})$, where the 2D map of the standard deviation of the noise $S_e(\mathbf{r})$ is calculated from emission-free end channels (in the case of GHIGLS, supplied with the archival data), and T_{sys} is the system temperature, typically 20 K for the GBT L-band observations. We used the augmented version of the ROHSA code employed by Taank et al. (2022) to work with 3D noise, rather than the standard 2D noise. For the DHIGLS data, we used the original implementation of ROHSA that considers $S_e(\mathbf{r})$.

4.2. GHIGLS

4.2.1. User parameters

⁴ NRAO VLA Sky Survey: <https://www.cv.nrao.edu/nvss>, Condon et al. (1998).

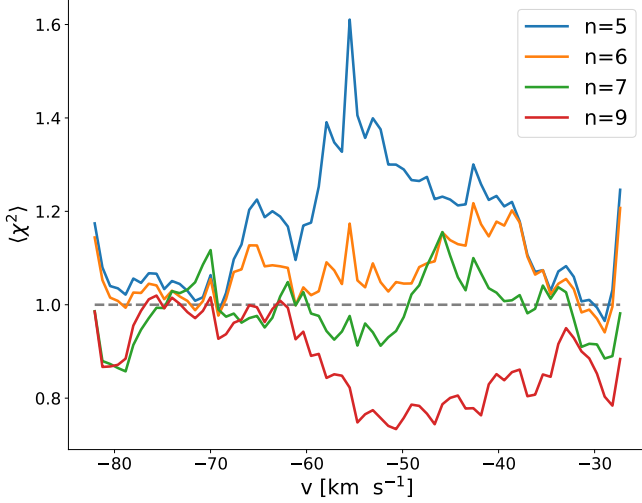


Figure 4. Spectrum of mean contribution to chi-square for Gaussian models fit with different numbers of Gaussians. Horizontal line indicates $\langle \chi^2 \rangle = 1$.

The representative solution presented in this work was obtained using the set of parameters $N = 6$, $\lambda_a = \lambda_\mu = \lambda_\sigma = 40$, and $\lambda''_\sigma = 50$.

To obtain a solution that fully describes the signal in the IVC range (i.e., LLIV1) without over-fitting the data, we found that $N = 6$ was optimal. This was accomplished by decomposing the data with varying N in the range $N = [5-9]$ and we used the per-channel mean contribution to chi-square,

$$\langle \chi^2(v) \rangle = \sum_r \left(\frac{L(v, \theta(r))}{S(v, r)} \right)^2 / 128^2, \quad (1)$$

to determine the goodness of fit, where $L(v, \theta(r))$ is the residual between the Gaussian model and the data. Here the fields $\theta_n(r) = (a_n(r), \mu_n(r), \sigma_n(r))$ – amplitude $a_n \geq 0$, mean velocity μ_n , and standard deviation σ_n – parameterize the N Gaussians of the model prescribed in ROHSA. Note that 128^2 is the total number of pixels inside the light blue box shown in Figure 1.

Figure 4 shows spectra of the mean contribution to chi-square $\langle \chi^2(v) \rangle$ for varying N , where $N = 6$ provides a solution in which $\langle \chi^2(v) \rangle$ is just slightly higher than unity denoted by the horizontal dashed line. For $N > 6$, $\langle \chi^2(v) \rangle$ is dominated by values lower than unity, especially where the signal is strong, which indicates over-fitting the data.

Figure 5 shows a reduced but spatially resolved version of Equation 1,

$$\chi_r^2(\theta(r)) = \sum_v \left(\frac{L(v, \theta(r))}{S(v, r)} \right)^2 / k, \quad (2)$$

where $k = 69 - 3N$ is the number of degrees of freedom, with 69 being the number of velocity channels. Spectral data

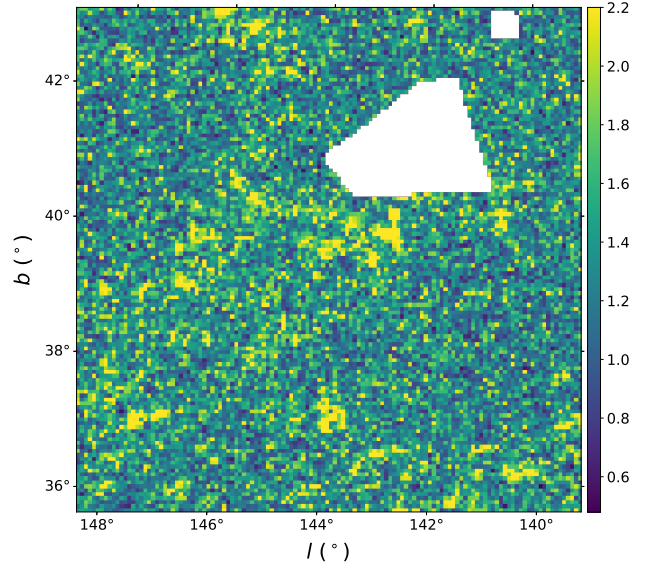


Figure 5. Map of the reduced χ_r^2 obtained with ROHSA on the GHIGLS data of LLIV1. Masked regions correspond to pixels contaminated by extragalactic emission and in-painted before decomposition.

that were in-painted prior to decomposing the cube was not considered and are shown as masked regions. Our best model achieves a mean χ_r^2 across the field of 1.4, with median and standard deviation of 1.3 and 0.4, respectively.

The four hyper-parameters that control the smoothness of the Gaussian parameter maps were chosen to be the same due to the similar functional form of their respective cost functions. This efficiency limits the parameter space explored in finding a practicable solution. They were chosen empirically to correlate adjacent pixels on a spatial scale close to the beam of the instrument. In experimenting with this set of parameters, the optimal model was found to have $\lambda_a = \lambda_\mu = \lambda_\sigma = 40$.

To ensure a solution in which phases are identifiable according to distinct velocity dispersions (phase separation), we explored a range of the λ''_σ parameter, which controls the variance of the normalized velocity dispersion of Gaussian components. We experimented with $\lambda''_\sigma = [1, 10, 20, 50, 100, 500, 1000]$ and found that 50 allows a coherent phase separation (see Section 4.2.2), without adding too much penalty in the global cost function prescribed in ROHSA that would prevent an overall good fit of the data.

4.2.2. A representative solution

The derived Gaussian model parameters for all spatial pixels are summarized in the 2D histogram of the column density weighted $\sigma - \mu$ parameters in Figure 6. There are six

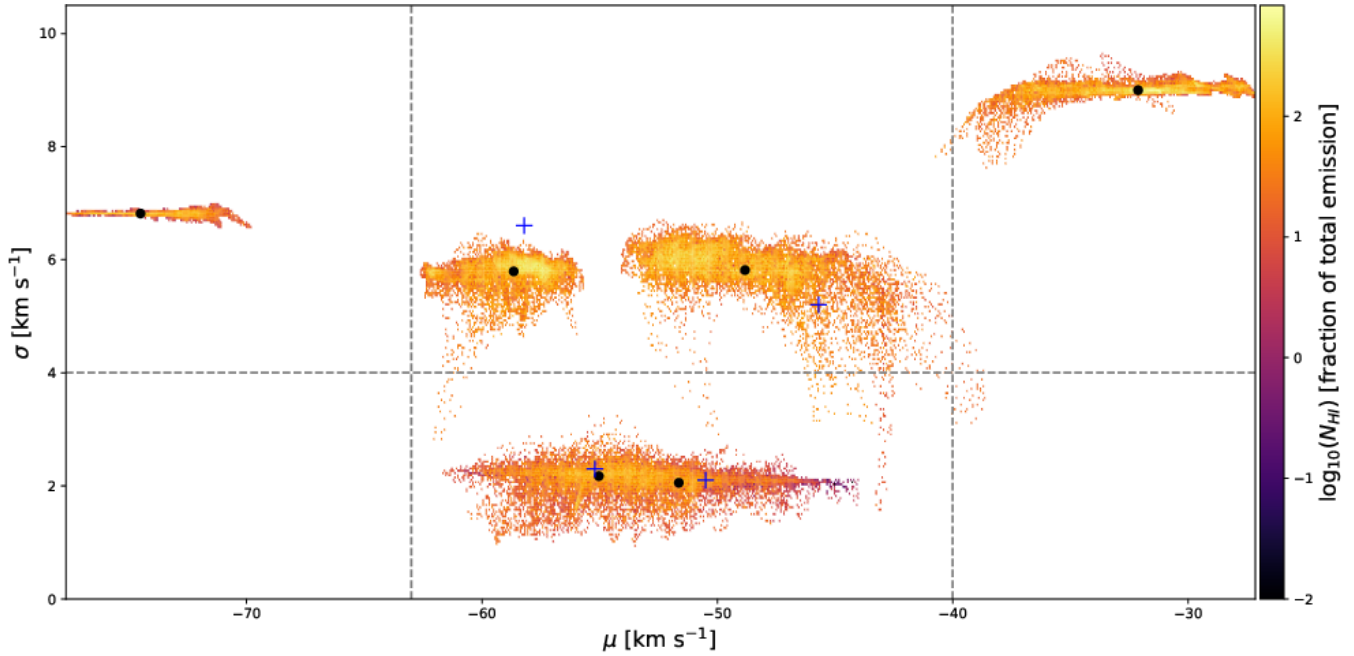


Figure 6. 2D histogram of σ and μ of the six Gaussians, weighted by their column densities obtained by decomposing the GHIGLS data of LLIV1 with ROHSA. The black dots correspond to the column density means of each cluster. The blue crosses show the same quantity but for the decomposition of the DHIGLS data within the selected velocity range. The horizontal dotted grey line shows the separation between the identified two thermal phases. The vertical grey lines show the velocity range where Gaussian components encodes emission from LLIV1.

Table 2. Mean kinematic properties (in km s^{-1}) of Gaussians encoding the IVC gas (LLIV1) in the GHIGLS and DHIGLS data

Survey		G_0	G_1	G_2	G_3	G_4	G_5
GHIGLS	$\langle \mu_n \rangle$	-73.6	-58.7	-55.6	-52.9	-48.7	-33.0
	$\langle \sigma_n \rangle$	6.8	5.7	2.1	2.0	5.8	9.08
DHIGLS	$\langle \mu_n \rangle$		-58.2	-55.2	-50.5	-45.7	-26.5
	$\langle \sigma_n \rangle$		6.6	2.3	2.1	5.2	10.0

clusters of points that correspond to the $N = 6$ Gaussians used by ROHSA to fit the data. Black points show the column density-weighted average of each cluster, as summarized in Table 2. The distinct average velocity dispersions of the six clusters, ranging from about two to nine km s^{-1} , reveal the multiphase nature of the gas in LLIV1.

We observe a clear separation of clusters vertically along the velocity dispersion axis, denoted by the grey horizontal dashed line. G_0 , G_1 , G_4 , and G_5 are broad, typical of warm gas, while G_2 and G_3 are narrow and can be associated with the cold phase of LLIV1. Interestingly, unlike what was found in other fields – LVC from GHIGLS in the North Ecliptic Pole (Marchal et al. 2019; Marchal & Miville-Deschênes 2021) and the NCPL (Taank et al. 2022), and HVC in complex C from DHIGLS in EN (Marchal et al. 2021) – there are no Gaussian components with intermediate dispersion characteristic of lukewarm gas (LNM) associated with a ther-

mally unstable medium. This suggests that in LLIV1 the thermal condensation and phase transition are not ongoing, but rather have reached an equilibrium state.

Horizontally, along the velocity axis, the components G_1 to G_4 are located near the peak of LLIV1 emission as shown in Figure 2. G_0 describes gas in the HVC range that is not of interest in this work and G_5 gas is located in the velocity bridge between emission from the LVC and LLIV1.

The corresponding Gaussian parameter maps, sorted by increasing mean velocity, are presented in Appendix A. Column density, velocity, and dispersion velocity maps of the six Gaussian components are shown in Figures A1, A2, and A3, respectively. Inspecting each column density map, we found that G_1 , G_2 , G_3 , and G_4 show a morphological correlation not shared with G_0 or G_5 . In the following sections, only the four Gaussian components between the two vertical dashed lines in Figure 6 were kept.

4.2.3. Uncertainties

To explore the degeneracy of the ROHSA solution, we generated a model cube from the mean representative solution, G_1 to G_4 in Table 2, and repeated the Gaussian decomposition using three series of 50 runs each (Marchal et al. 2021; Taank et al. 2022). The first series explored how the outcome of the decomposition was influenced by the injection of 50 different instances of noise. The hyper-parameters were kept the same. The second series explored the impact of the hyper-parameters, with 50 runs using random perturba-

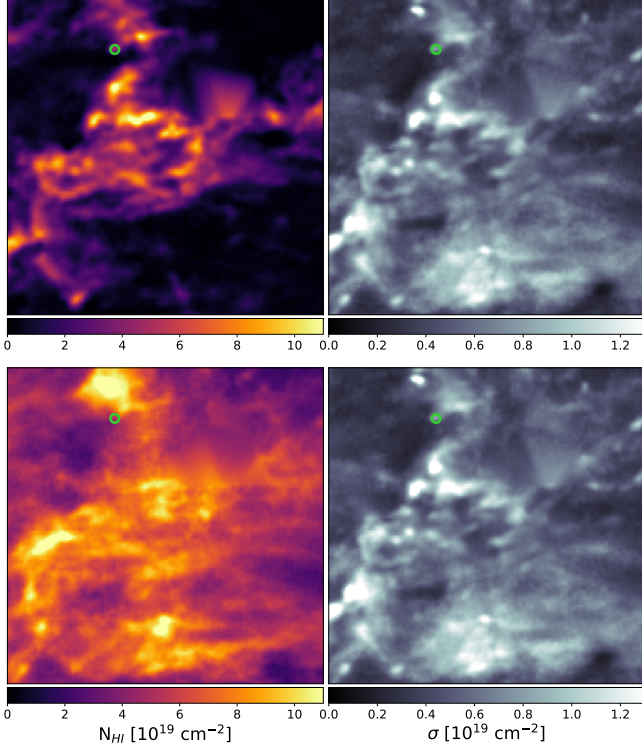


Figure 7. Column density maps (first column) with their associated uncertainties (second column) of the cold (top) and warm (bottom) phases in the GHIGLS data of LLIV1. The green ring marks the position of the absorption feature against 4C +66.09.

tions of the four ROHSA hyper-parameters in a $\pm 10\%$ interval around the original values. Here, the injected noise was kept the same. The third explored the sensitivity to the four Gaussians needed to initialize ROHSA, with 50 runs selecting them randomly from the original $\sigma - \mu$ diagram in Figure 6. We refer the reader to Taank et al. (2022) for further details of that procedure.

For each of the 50-run series, the outcomes were examined in $\sigma - \mu$ space, revealing that the clusters observed as in Figure 6 were quite stable, including the lack of components with intermediate velocity dispersions. For each run, we performed a phase separation by grouping the four Gaussians into two categories based on their mean velocity dispersion; Gaussians with $\langle \sigma_n \rangle > 4 \text{ km s}^{-1}$ were classified as WNM and Gaussians with $\langle \sigma_n \rangle < 4 \text{ km s}^{-1}$ were classified as CNM.

For each series, maps of the mean column density and its standard deviation were generated for the two components. Results from all 150 runs were combined to calculate the final maps of the column density for the two components. For both of these, the standard deviations from the three series were summed in quadrature to yield the total uncertainty.

4.2.4. Phase maps

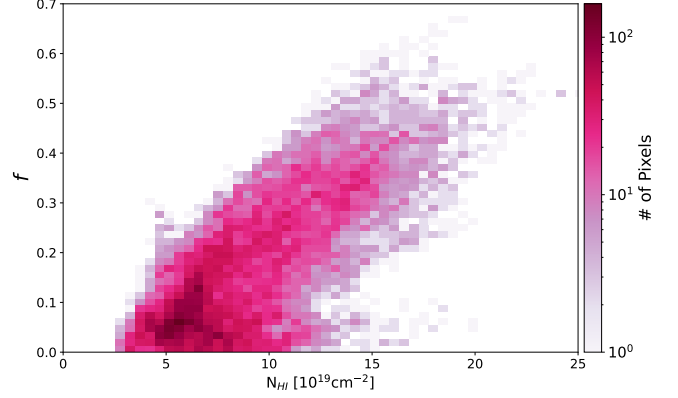


Figure 8. 2D histogram of the CNM mass fraction with respect to the total N_{HI} , from the GHIGLS solution.

Figure 7 shows the column density maps (first column) with their associated uncertainty maps (second column) of the cold (top) and warm phases (bottom) in the GHIGLS data of LLIV1. There are some variations of the uncertainties across the field, but the low values of the uncertainties relative to the associated column densities indicate the good stability of the solution found with ROHSA.

The cold phase of LLIV1 appears as a collection of elongated filaments that forms a closed structure within the decomposed field. These substructures follow the orientation of the overall large-scale cloud, along the diagonal of the field from the northwest to the southeast (Galactic coordinates). The column density of the more diffuse warm phase is highest within the contour delimited by the presence of cold gas but also exists outside of LLIV1.

Statistically, the cold gas mass fraction f increases with the total gas column density, as seen in the 2D histogram in Figure 8.⁵ In physical structures like in LLIV1, increases in column density are likely indicative of increased volume density, rather than increased path length along the line of sight. Thus the trend in Figure 8 suggests that f increases with volume density. In any instability leading to CNM, cooling relative to heating increases most rapidly in dense gas, increasing the efficiency and shortening the timescale of thermal condensation. Perhaps this is an intuitive basis for the trend, but numerical simulations would be needed for a full understanding. Beyond what is seen statistically in Figure 8, the spatial dependence of (high) f will be quantified in Section 4.3.4.

4.2.5. Power spectrum

We statistically quantified and compared the multi-scale structure of the two phases by calculating for each the angular power spectrum $P(k)$, the azimuthal average of the modulus

⁵ Note that if $f \propto N_{\text{HI}}(\text{total})$ then $N_{\text{HI}}(\text{CNM}) \propto N_{\text{HI}}(\text{total})^2$, which non-linearity is borne out in the alternative 2D histogram $N_{\text{HI}}(\text{CNM})$ vs. $N_{\text{HI}}(\text{total})$ (not shown).

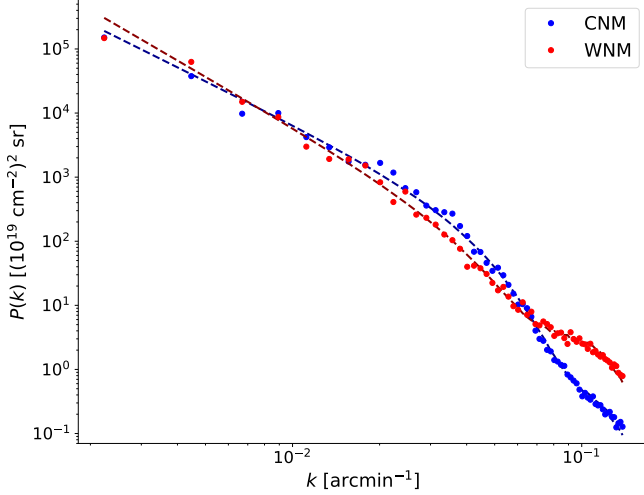


Figure 9. Angular power spectra $P(k)$ of the integrated column density of the cold (blue) and warm (red) phases. The dashed lines represent the models fit to each phase independently.

of the Fourier transform of the column density field. Following [Martin et al. \(2015\)](#) and [Blagrove et al. \(2017\)](#), we modelled them as $P(k) = B(k) \times P_0 k^\gamma + A \times N(k)$, where P_0 is the amplitude of the power spectrum, γ is the scaling exponent, $B(k)$ describes the cutoff of the spectrum at high k due to the beam of the instrument, assumed to be a 2D Gaussian of FWHM = 9.4, and $N(k)$ is the noise estimated by taking the power spectrum of empty channel maps of the PPV cube and scaled by a multiplicative factor A . The finite images were apodized using a cosine function to minimize systematic edge effects in the implementation of the Fourier transform.

Figure 9 shows $P(k)$ for the cold and warm phases, in blue and red dots respectively. The total fitted model is shown by the dashed dark blue and red curves for the cold and warm phases, respectively. Recognizing the uncertainties, we find that the scaling exponent for the cold phase $\gamma_{\text{CNM}} = -2.230 \pm 0.002$ is higher than that of the warm phase with $\gamma_{\text{WNM}} = -2.613 \pm 0.003$. In other words, the power spectrum of the cold phase is slightly shallower than that of the warm phase, quantifying that the cold phase has relatively more structure on small scales. This is similar to what was found in high latitude LVC gas in the NEP field of the GHIGLS survey ([Marchal & Miville-Deschênes 2021](#)) and in HVC gas (complex C) in the EN field of the DHIGLS survey ([Marchal et al. 2021](#)).

4.3. DHIGLS

4.3.1. Initialization

We performed a first exploration of the user parameters using the same methodology as described in Section 4.2.1. This search resulted in a set of parameters ($N = 5$, $\lambda_a =$

$\lambda_\mu = \lambda_\sigma = 10$, and $\lambda''_\sigma = 10$) that could satisfy our selection criteria, including a flat χ_r^2 map with a mean value close to unity. Although statistically good, this solution was found to be inadequate. After generating the model cube from the solution and applying a convolution to both the model and the data to lower their spatial resolution, the model was no longer providing a good description of the data.

Specifically, on some lines of sight where the convolved data show two distinct peaks even at a resolution as low as 2', the model solution was found to have only one narrow Gaussian to describe the cold gas. Figure B1 illustrates the spectrum on such a line of sight, showing the original data (black) and the data convolved to 2' and 9.4 resolution in green and blue, respectively. The improved model, described next, fit to the DHIGLS data is shown by the red curve.

To obtain a consistent solution at various resolution (from the native 1' beam to the 9.4 beam of the GHIGLS data), we used the GHIGLS values tabulated in Table 2 as initial parameters to start the multi-resolution process prescribed in ROHSA ([Marchal et al. 2019](#); [Taank et al. 2022](#)). Only the five components whose mean velocities were included in the velocity range covered by the DHIGLS data were used: Gaussians G_1 to G_5 .

4.3.2. Solution and Uncertainties

An appropriate set of hyper-parameters was again found to be $\lambda_a = \lambda_\mu = \lambda_\sigma = 10$, and $\lambda''_\sigma = 10$. The resulting decomposition still satisfies all of our selection criteria, with a fairly uniform χ_r^2 map (not shown here) and showing no evidence of over-fitting the data.

The mean kinematic properties of the five Gaussians used to describe the DHIGLS data are tabulated in Table 2. Values of the components G_1 to G_4 (associated with LLIV1) are also denoted by blue crosses in Figure 6, appearing to be fairly consistent with those obtained from the decomposition of the GHIGLS data.

The corresponding parameter maps of the five Gaussian components, column density, velocity, and velocity dispersion, sorted by increasing mean velocity, are presented in Appendix C, Figure C1. Inspection of each column density map shows similar morphology (and morphological correlation between components) to those of the GHIGLS solution, described in Section 4.2.2 and Appendix A.

Building on this solution, we followed the same methodology as described in Section 4.2.3 to evaluate the mean column density and uncertainty maps for each phase. The top and bottom panels in Figure 10 show the resulting maps for the cold and warm phases, respectively.

4.3.3. Comparison with GHIGLS

Our modeling of the cold phase in LLIV1 at high resolution (1') reveals similar large scale properties as the 9.4 modeling obtained with GHIGLS data; the cold phase seems to be

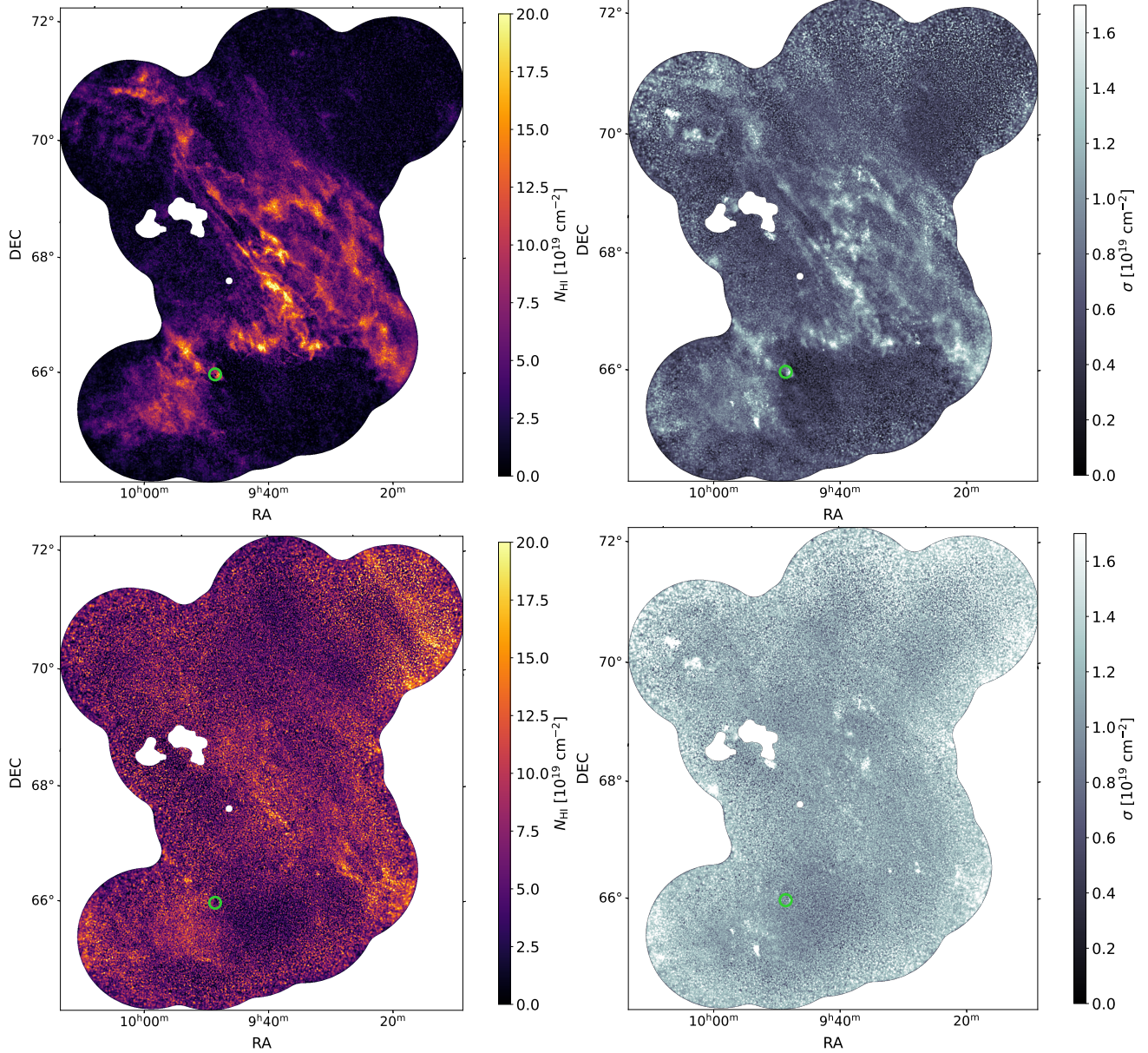


Figure 10. Column density maps (first column) with their associated uncertainty maps (second column) of the cold (top) and warm (bottom) phases from the DHIGLS data in LLIV1. The green ring marks the position of the absorption measurement against 4C +66.09.

confined within a closed contour, surrounded by or mixed in with its warm counterpart. The global orientation of LLIV1 and the filamentary structures within suggests that there is a bulk motion of the gas cloud on the plane of the sky (from top left to bottom right in Equatorial coordinates).

The cold filamentary structures appear thinner at this resolution and the width of some filaments likely reaches the size of the $1'$ beam of the DHIGLS data. This is notably the case for the highly elongated filament seen just to the right of the masked regions within the field and oriented along its diagonal (from top left to bottom right). Clustering the filaments and analyzing their statistical properties (Marchal et al. 2021)

is beyond the scope of this paper but in further work would provide valuable insight into the thermal condensation that has occurred in LLIV1.

4.3.4. CNM mass fraction

The left panel in Figure 11 shows our best model of the cold gas mass fraction $f(r)$ in LLIV1 at the $1'$ resolution of the DHIGLS data, and the left panel shows the corresponding uncertainties. Large variations of $f(r)$ occur across the field and even within the contour delimiting the large scale extent of the cold phase. The mean and standard deviation of $f(r)$ are 0.33 and 0.19, respectively. Interpolated at the position

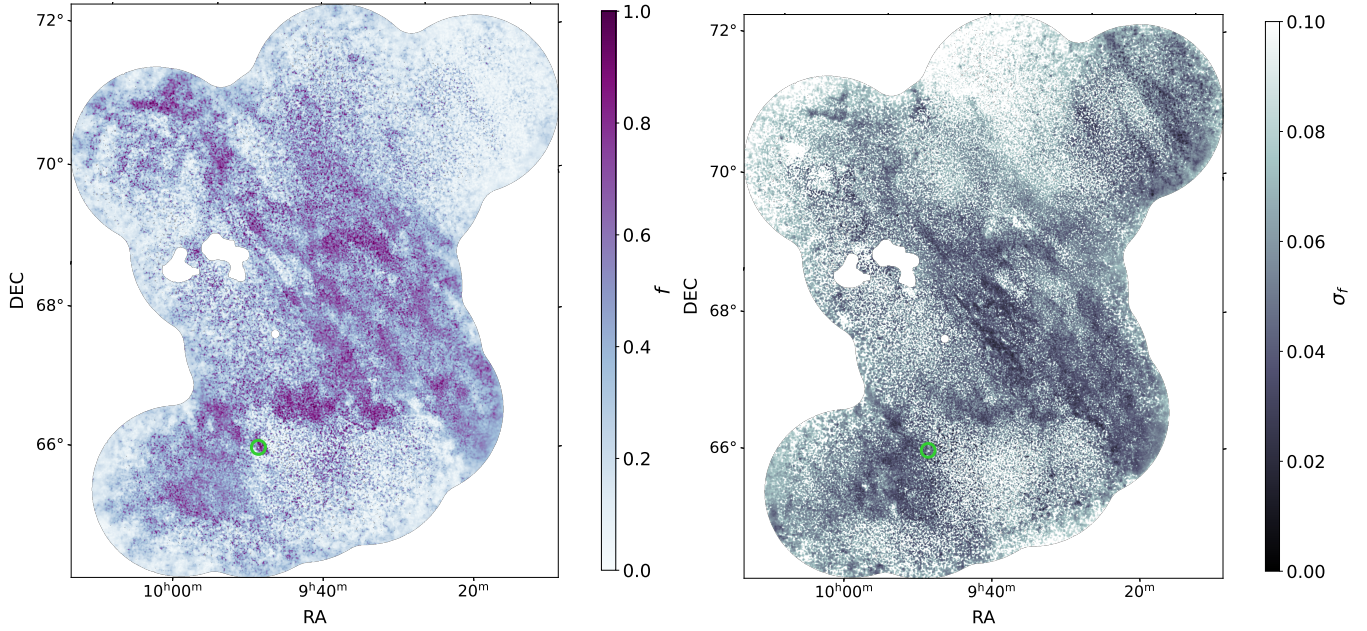


Figure 11. CNM mass fraction map and uncertainty inferred from the DHIGLS data.

of the absorption measurement against $4C +66.09$, $f(\mathbf{r})$ is 0.46 ± 0.06 , close to the values tabulated in Table 1.

The spatial distribution (i.e., morphological structure) of $f(\mathbf{r})$ resembles the column density map of the cold phase only, due to a relatively constant (i.e., flat) column density observed in the warm phase within the sky coverage of the DHIGLS data. Specifically, $f(\mathbf{r})$ shows the same elongated filaments, as well as finger-like structures that seem to be part of an organized series of scalloping structures at the implied leading edge of LLIV1, oriented perpendicular to the large-scale orientation of the cloud and large filaments. This is reminiscent of the structures observed in the Draco Nebula (Miville-Deschênes et al. 2017, and references therein), another IVC that is thought to be part of the Galactic fountain process.

5. SUMMARY

Our novel study of the multi-phase properties of LLIV1 is based on H I spectra from GHIGLS and DHIGLS. We used ROHSA to decompose the spectral data in emission to model their multiphase structure and corroborated this with analysis of an absorption spectrum. The main conclusions are as follows.

- From the absorption line measurement in LLIV1 against $4C +66.09$, we find spin temperature $T_s \sim 75$ K, cold gas mass fraction $f \sim 0.5$ (with no component associated with a thermally unstable medium), and turbulent sonic Mach number $M_t \sim 3.4$, characteristic of supersonic turbulence in the cold phase.
- Similar to the absorption line modeling against $4C +66.09$, our best emission line decomposition

model has no unstable gas across the whole field of view, suggesting that the thermal condensation and phase transition are not on-going but rather have reached an equilibrium state.

- The cold phase of LLIV1 appears as a collection of elongated filaments that forms a closed structure within the field decomposed. These substructures follow the orientation of the overall large scale cloud, along the diagonal of the GHIGLS field from north-west to south-east (in Galactic coordinates).
- The column density of the more diffuse warm phase is highest within the contour delimiting the presence of cold gas, but also exists outside of LLIV1.
- The angular power spectrum of the cold phase is slightly shallower than that of the warm phase, quantifying that the cold phases have relatively more structure on small scales.
- Our spatially resolved map of the cold gas mass fraction in LLIV1 is consistent with the absorption measurement against $4C +66.09$ and reveals significant variations spanning the possible range of f , with mean and standard deviation of 0.33 and 0.19, respectively.

ACKNOWLEDGMENTS

We acknowledge support from the Natural Sciences and Engineering Research Council (NSERC) of Canada. Some of this work was carried out when LV and MT participated in the Summer Undergraduate Research Program (SURP) hosted by the University of Toronto. This research made use of the NASA Astrophysics Data System.

Software: Matplotlib ([Hunter 2007](#)), NumPy ([van der Walt et al. 2011](#)), and AstroPy⁶, a community-developed core Python package for Astronomy ([Astropy Collaboration et al. 2013, 2018](#)), SciPy ([Virtanen et al. 2020](#)), scikit-image ([van der Walt et al. 2014](#)).

⁶ <http://www.astropy.org>

APPENDIX

A. PARAMETER MAPS OF INDIVIDUAL GAUSSIAN COMPONENTS (GHIGLS)

Figure A1 shows the column density maps of each Gaussian sorted by increasing column density-weighted mean velocities (see Table 2). Figures A2 and A3 shows the corresponding velocity fields and velocity dispersion fields. Note the shifting ranges of the color bars, as described in the captions.

The labels overlaid on the panels in Figure A1 associate them with the clusters in Figure 6; e.g., for G_2 (in row 2, column 1), “ G_2 CNM 2.1” indicates the number of the Gaussian component, the thermal phase, and the column density-weighted mean velocity dispersion (σ_n) in km s^{-1} as tabulated in Table 2. $G_1 - G_4$ are the components of interest for the IVC gas in LLIV1. G_0 and G_5 are important for the ROHSA decomposition, but not particularly meaningful for the IVC analysis.

The white contour outlines the DHIGLS UM field (Section 2.2 and Appendix C) and also serves a fiducial role spatially.

B. IMPACT OF SPATIAL RESOLUTION ON THE LINE

Figure B1 illustrates the impact of spatial resolution on a line of sight within the DHIGLS field chosen for its distinct double peak property. The black curve shows the original DHIGLS data, and the green and blue curves show the same data convolved to $2'$ and $9'.4$, respectively. The ROHSA model fit to the original DHIGLS data at $1'$ resolution (red curve) captures the double-peak structure using two narrow Gaussians.

C. PARAMETER MAPS OF INDIVIDUAL GAUSSIAN COMPONENTS (DHIGLS)

These are all arrayed in Figure C1. Note the shifting color bars. $G_1 - G_4$ are the components of interest for the IVC gas in LLIV1. G_5 is important for the ROHSA decomposition, but not particularly meaningful for the IVC analysis.

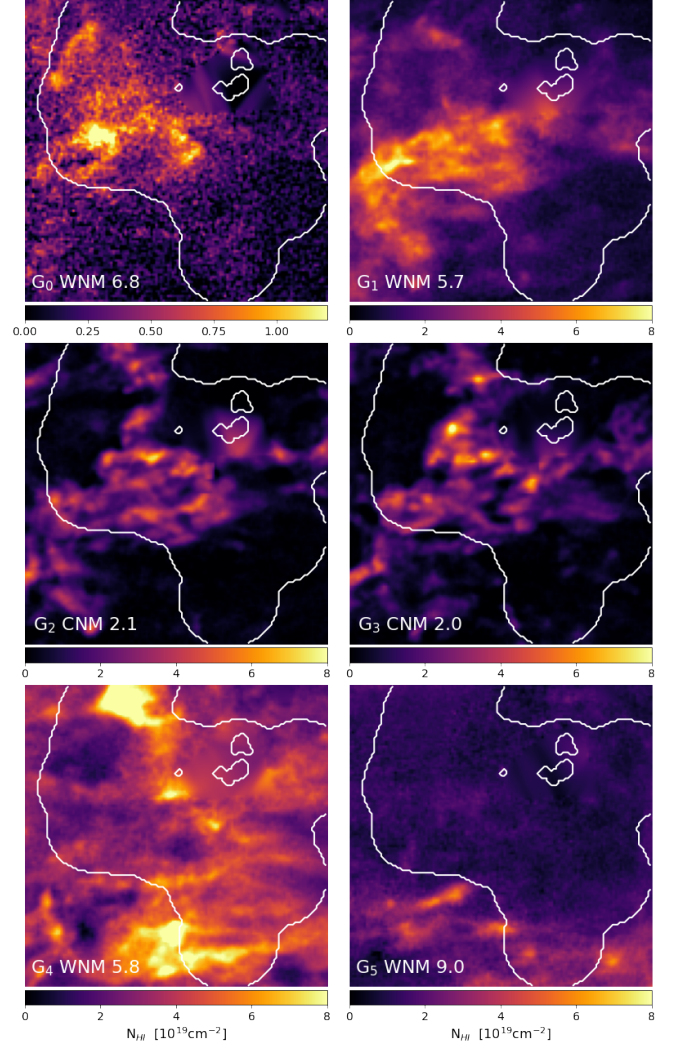


Figure A1. Mosaic of N_{HI} maps of the individual Gaussian components. The maps are sorted by mean velocity. The white contour outlines the DHIGLS UM field (Section 2.2). The labels in the bottom left corner represent the classification of that particular Gaussian component. The number is the mean velocity dispersion (σ) in units of km s^{-1} . See Table 2 and Figure 6, which shows that $G_1 - G_4$ are the components of interest for the IVC gas in LLIV1. The range of the color bar is the same for $G_1 - G_5$, chosen to reveal the spatial structure and to emphasize the relative importance of the components across the region. Component G_0 is very weak and the color bar chosen has a much smaller range.

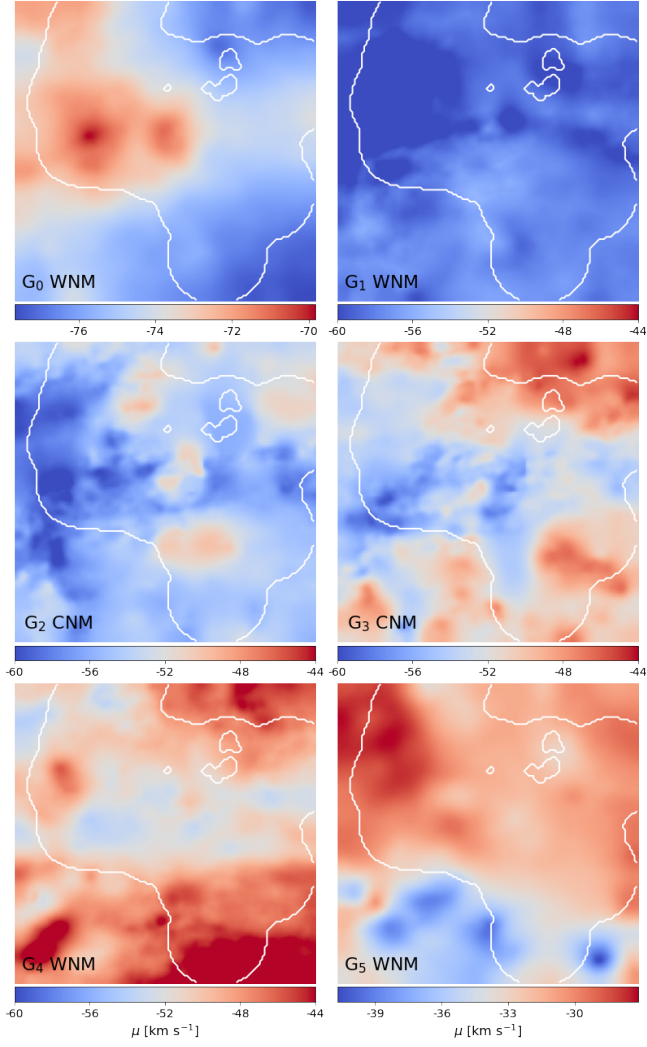


Figure A2. Mosaic like Fig. A1, but of maps of the mean velocity μ of the Gaussian components. The range of the color bar is the same for $G_1 - G_4$. However, G_0 and G_5 are disjoint and the ranges of their color bars are chosen to show the spatial structure.

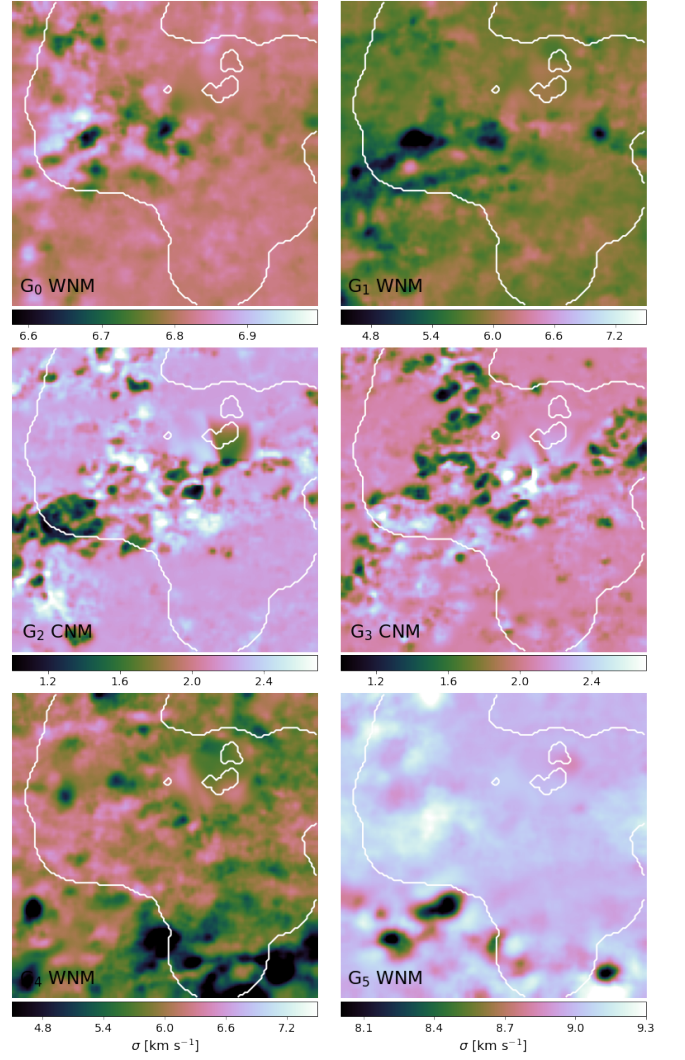


Figure A3. Mosaic like Fig. A1, but of maps of the velocity dispersion σ of the Gaussian components. The range of the color bar is the same for the CNM components G_2 and G_3 . Likewise, the WNM components G_1 and G_4 share the same range. However, G_0 and G_5 are disjoint and the ranges of their color bars are chosen to show the spatial structure.

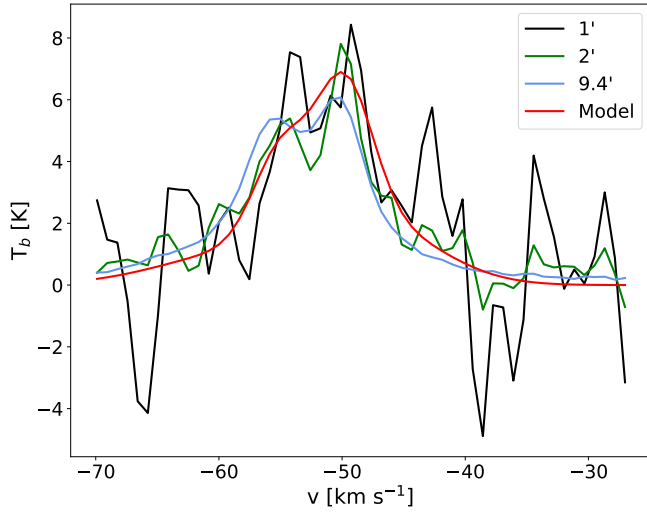


Figure B1. Spectrum showing a double peak of cold gas within the DHIGLS field. The black curve shows the original DHIGLS data, and the green and blue curves show the same data convolved to 2' and 9.4', respectively. The red curve shows the model fit to the original DHIGLS data at 1' resolution.

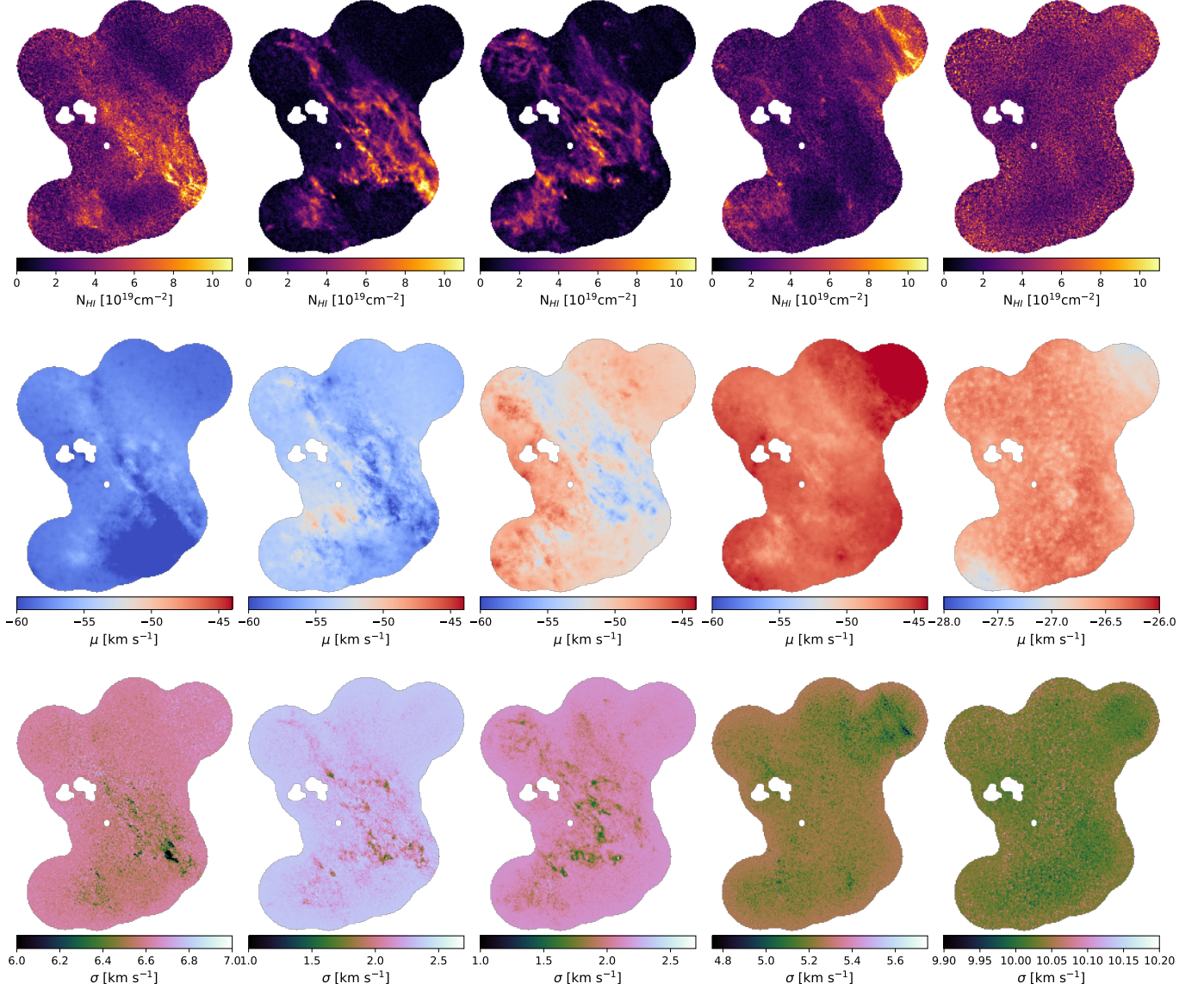


Figure C1. N_{HI} and parameter maps of Gaussian components $G_1 - G_5$ (Table 2) identified in the analysis of IVC gas from the DHIGLS data, $G_1 - G_4$ being the components of interest for LLIV1. Top: column density N_{HI} , all with the same color bar range. Middle: corresponding mean velocity field μ . The range of the color bar is the same for $G_1 - G_4$ and identical to that in Figure A2. G_5 is disjoint. Bottom: velocity dispersion σ . The range of the color bar is the same for the CNM components G_2 and G_3 and identical to that in Figure A3. The WNM components G_1 and G_4 are sufficiently different that we chose separate narrow ranges, both within the common range for the G_1 and G_4 components in Figure A3, so as not to suppress spatial structure. G_5 is disjoint.

REFERENCES

- Astropy Collaboration, Robitaille, T. P., Tollerud, E. J., et al. 2013, A&A, 558, A33, doi: [10.1051/0004-6361/201322068](https://doi.org/10.1051/0004-6361/201322068)
- Astropy Collaboration, Price-Whelan, A. M., Sipőcz, B. M., et al. 2018, AJ, 156, 123, doi: [10.3847/1538-3881/aabc4f](https://doi.org/10.3847/1538-3881/aabc4f)
- Blagrove, K., Martin, P. G., Joncas, G., et al. 2017, ApJ, 834, 126, doi: [10.3847/1538-4357/834/2/126](https://doi.org/10.3847/1538-4357/834/2/126)
- Boothroyd, A. I., Blagrove, K., Lockman, F. J., et al. 2011, A&A, 536, A81, doi: [10.1051/0004-6361/201117656](https://doi.org/10.1051/0004-6361/201117656)
- Bregman, J. N. 1980, ApJ, 236, 577, doi: [10.1086/157776](https://doi.org/10.1086/157776)
- Condon, J. J., Cotton, W. D., Greisen, E. W., et al. 1998, AJ, 115, 1693, doi: [10.1086/300337](https://doi.org/10.1086/300337)
- de Boer, K. S., Rodriguez Pascual, P., Wamsteker, W., et al. 1993, A&A, 280, L15
- Houck, J. C., & Bregman, J. N. 1990, ApJ, 352, 506, doi: [10.1086/168554](https://doi.org/10.1086/168554)
- Hunter, J. D. 2007, CSE, 9, 90, doi: [10.1109/MCSE.2007.55](https://doi.org/10.1109/MCSE.2007.55)
- Kuntz, K. D., & Danly, L. 1996, ApJ, 457, 703, doi: [10.1086/176765](https://doi.org/10.1086/176765)
- Marchal, A., Martin, P. G., & Gong, M. 2021, ApJ, 921, 11, doi: [10.3847/1538-4357/ac0e9d](https://doi.org/10.3847/1538-4357/ac0e9d)
- Marchal, A., & Miville-Deschênes, M.-A. 2021, ApJ, 908, 186, doi: [10.3847/1538-4357/abd108](https://doi.org/10.3847/1538-4357/abd108)
- Marchal, A., Miville-Deschênes, M.-A., Orioux, F., et al. 2019, A&A, 626, A101, doi: [10.1051/0004-6361/201935335](https://doi.org/10.1051/0004-6361/201935335)
- Martin, P. G., Blagrove, K. P. M., Lockman, F. J., et al. 2015, ApJ, 809, 153, doi: [10.1088/0004-637X/809/2/153](https://doi.org/10.1088/0004-637X/809/2/153)
- Miville-Deschênes, M. A., Salomé, Q., Martin, P. G., et al. 2017, A&A, 599, A109, doi: [10.1051/0004-6361/201628289](https://doi.org/10.1051/0004-6361/201628289)
- Normandeau, M., Taylor, A. R., & Dewdney, P. E. 1996, Nature, 380, 687, doi: [10.1038/380687a0](https://doi.org/10.1038/380687a0)
- Planck Collaboration XXIV. 2011, A&A, 536, A24, doi: [10.1051/0004-6361/201116485](https://doi.org/10.1051/0004-6361/201116485)
- Richter, P., Savage, B. D., Wakker, B. P., Sembach, K. R., & Kalberla, P. M. W. 2001, ApJ, 549, 281, doi: [10.1086/319070](https://doi.org/10.1086/319070)
- Richter, P., Wakker, B. P., Savage, B. D., & Sembach, K. R. 2003, ApJ, 586, 230, doi: [10.1086/346204](https://doi.org/10.1086/346204)
- Shapiro, P. R., & Field, G. B. 1976, ApJ, 205, 762, doi: [10.1086/154332](https://doi.org/10.1086/154332)
- Stark, A. A., Gammie, C. F., Wilson, R. W., et al. 1992, ApJS, 79, 77, doi: [10.1086/191645](https://doi.org/10.1086/191645)
- Taank, M., Marchal, A., Martin, P. G., & Vujeva, L. 2022, ApJ, 937, 81, doi: [10.3847/1538-4357/ac8b86](https://doi.org/10.3847/1538-4357/ac8b86)
- van der Walt, S., Colbert, S. C., & Varoquaux, G. 2011, CSE, 13, 22
- van der Walt, S., Schönberger, J. L., Nunez-Iglesias, J., et al. 2014, PeerJ, 2, e453, doi: [10.7717/peerj.453](https://doi.org/10.7717/peerj.453)
- Virtanen, P., Gommers, R., Oliphant, T. E., et al. 2020, Nature Methods, 17, 261, doi: <https://doi.org/10.1038/s41592-019-0686-2>
- Wakker, B. P. 2001, ApJS, 136, 463, doi: [10.1086/321783](https://doi.org/10.1086/321783)